Check for updates

Scalable fabrication of high-quality crystalline and stable FAPbI₃ thin films by combining doctor-blade coating and the cation exchange reaction†

Sampson Adjokatse, [ID] Hong-Hua Fang, [ID] Herman Duim [ID] and Maria Antonietta Loi [ID] *

Formamidinium lead iodide (FAPbI₃) is one of the most extensively studied perovskite materials due to its narrow band gap and high absorption coefficient, which makes it highly suitable for optoelectronic applications. Deposition of a solution containing lead iodide (PbI₂) and formamidinium iodide (FAI) or sequential deposition of PbI₂ and FAI usually leads to the formation of films with a poor morphology and an unstable crystal structure that readily crystallize into two different polymorphs: the photoinactive yellow phase and the photoactive black phase. In this work, 2D 2-phenylethylammonium lead iodide (PEA₂PbI₄) thin films are deposited by a scalable doctor-blade coating technique and used as a growth template for the high-quality 3D FAPbI₃ perovskite thin films which are obtained by organic cation exchange. We report the structural, morphological and optical properties of these converted 3D FAPbI₃ perovskite films which we compare to the directly deposited 3D FAPbI₃ films. The converted FAPbI₃ thin films are compact, smooth, and highly oriented and exhibit better structural stability in comparison with the directly deposited 3D films. These results not only underscore the importance of the employed deposition techniques in fabricating highly crystalline and stable perovskite thin films but also provide a strategy to easily obtain very compact perovskite layers using doctor-blade coating.

Introduction

Organic–inorganic metal halide perovskite semiconductors are of very high interest to the semiconductor community due to their superior photophysical properties and their ever-increasing significance for optoelectronic and other electronic applications.[1–4] Thin films of metal halide perovskites have been used extensively as light absorbers in photovoltaics[5–8] with a certified record power conversion efficiency (PCE) of 23.7%.[9] Other optoelectronic devices in which perovskite semiconductors have been investigated and that have demonstrated outstanding performances include light-emitting diodes,[10–12] light-emitting field-effect transistors,[13–16] lasers,[17–20] photodetectors[21–25] and X-ray detectors.[26,27]

One of the key factors central to the demonstrated device performances is the perovskite film quality. This includes the morphology, crystallinity and phase purity. In the last few years, the most used deposition method has been the one-step solution processing technique, which involves direct deposition of a solution containing the perovskite precursors, typically lead halide (PbX₂, X = I⁻, Br⁻, or Cl⁻) and methyl-

ammonium halide (MAX) or formamidinium halide (FAX).[3,28] This technique results in the formation of thin films with a poor surface coverage, a large surface roughness and often unreacted PbX₂ residues, with negative consequences for the performance and stability of devices.[29] To enhance the perovskite film quality, deposition techniques such as the two-step sequential deposition, vapor-assisted deposition, and thermal vapor deposition techniques have been developed.[30–34] Other techniques such as solvent engineering,[35–37] solvent additives[38] or temperature-assisted rapid nucleation[39] and process engineering methods like anti-solvent treatment,[40] solvent annealing[41] and hot-casting[42] have all been developed in order to control the film morphology and its quality in general.

An important problem is that the quality of the films deposited by these techniques is strongly dependent on the material composition and the solvent used, which is one of the main reasons for the large proliferation of deposition techniques. For instance, while high-quality perovskite films of methylammonium lead iodide (MAPbI₃) have been prepared using most of the abovementioned advanced processing techniques, only the sequential deposition method has given satisfactory formamidinium lead iodide (FAPbI₃) thin films.[43–47]

FAPbI₃ is a highly interesting material because of its band gap (~1.48 eV) and its enhanced thermal stability compared to the widely used MAPbI₃. However, the ionic radius and symmetry of the FA⁺ cation make the FAPbI₃ perovskite structurally

Zernike Institute for Advanced Materials, University of Groningen, Nijenborgh 4, 9747 AG Groningen, The Netherlands. E-mail: m.a.loi@rug.nl
†Electronic supplementary information (ESI) available. See DOI: 10.1039/c8nr10267h

unstable as it can readily crystallize into two different polymorphs at room temperature: the undesired photoinactive "yellow" δ-phase (δ-FAPbI$_3$) and the desired photoactive "black" α-phase (α-FAPbI$_3$).[47,48] Thus, new strategies are required to fabricate and scale up high-quality FAPbI$_3$ thin films with improved morphology and structural stability, which could lead to enhanced optoelectronic properties, both in terms of performances and stability.

Recently, an avalanche of new processing techniques has been employed to control and grow high-quality perovskite thin films and to tune their composition. One such technique is the incorporation of dopants such as Cs to structurally stabilize FAPbI$_3$ as demonstrated by Zhu and co-workers.[49] An alternative technique is the ion exchange reaction, which is a well-known method for engineering material composition, creating alloys or obtaining controlled doping.[50] MAPbI$_3$ thin films with high surface coverage, smoothness and crystallinity have been successfully fabricated using various starting materials as thin film growth templates.[51–54] Similarly, using HPbI$_3$, NH$_4$PbI$_3$,[55] MAPbI$_3$[56] etc. as growth templates, various groups have demonstrated the fabrication of phase-pure α-FAPbI$_3$ thin films with enhanced film quality. Eperon et al. have also successfully demonstrated the exchange of the B-site metal cation by partial or full substitution of the tin (Sn) in formamidinium tin iodide (FASnI$_3$) with lead (Pb).[57] Jen and co-workers recently used a 2D perovskite, namely, phenylethylammonium lead bromide (PEA$_2$PbBr$_4$), as a growth template, obtaining highly oriented, high-quality 3D methylammonium lead bromide (MAPbBr$_3$) thin films.[58]

At this point, it is important to underline that all these techniques are based on a spin coating step and are difficult or impossible to scale up, which is a bottleneck towards the exploitation of hybrid perovskites in technology. Given the need for solution-based thin film deposition techniques that are simple, low-cost and compatible with industrial-scale fabrication, in this work we demonstrate an industrially relevant deposition pathway giving rise to high quality hybrid perovskite thin films. This deposition pathway combines the advantages of doctor-blade coating and the ion exchange reaction method to fabricate high-quality phase-pure α-FAPbI$_3$ perovskite thin films that are structurally stable and highly crystalline. Phenylethylammonium lead iodide (PEA$_2$PbI$_4$) perovskite thin films are doctor-blade coated and fully converted to α-FAPbI$_3$ upon immersing the 2D layer in a FAI solution. The choice of PEA$_2$PbI$_4$ as our starting material is based on its good film formability on different substrates even when deposited using different deposition techniques, including scalable blade coating. For comparison, one-step doctor-blade coated FAPbI$_3$ thin films are also investigated. The structural, morphological and optical characterization shows that the converted thin films exhibit unprecedented film quality, with preferential crystallographic orientation and enhanced ambient stability compared to the one-step deposited films. These results underline the immense potential of combining the scalable doctor-blade coating and the ion exchange reaction technique in the growth of stable and high-quality perovskite thin films.

Experimental

Materials and solution preparation

The perovskite precursors lead(II) iodide (PbI$_2$) (99.99%), 2-phenylethylammonium iodide (C$_6$H$_5$C$_2$H$_4$NH$_3$I, PEAI) (>98%) and formamidine hydroiodide (FAI) (>98%) were purchased from TCI EUROPE N.V. and used as received without further purification. N,N'-Dimethylformamide (DMF) (99.8%) was acquired from Sigma-Aldrich and dimethyl sulfoxide (DMSO) (99.9%) from Alfa Aesar.

The 2D PEA$_2$PbI$_4$ perovskite precursor solution was prepared by dissolving PEAI and PbI$_2$ at a molar ratio of 2:1 in a mixed solvent of DMF and DMSO at a volume ratio of 4:1 to form a solution of 0.5 M concentration. The 3D FAPbI$_3$ perovskite precursor solution was prepared by dissolving FAI and PbI$_2$ at a molar ratio of 1:1 also in a mixed solvent of DMF and DMSO at a volume ratio of 4:1 to form a solution of 1 M concentration. The solutions were stirred for at least 3 hours at room temperature before deposition. The organic precursor solution was prepared by dissolving FAI in isopropyl alcohol (IPA) to form a solution with a concentration of 20 mg mL^{-1}.

Perovskite film fabrication

The films were fabricated on glass substrates, which were ultrasonically cleaned in detergent solution, deionized water, acetone and isopropanol, sequentially. After drying them in an oven at 140 °C for about 10 min, they were treated with ultraviolet ozone (UV-O$_3$) for 20 min and then transferred to a nitrogen-filled glove box immediately for film deposition.

The perovskite growth process involved the transformation of the pure 2D perovskite PEA$_2$PbI$_4$ into the desired 3D FAPbI$_3$ perovskite thin film by the ion exchange method. The 2D films were fabricated using the spin coating and doctor blade coating techniques. The spin coated 2D samples were fabricated using a two-step spin program with anti-solvent treatment. The spin program was set at 1000 rpm for 10 s and 4000 rpm for 30 s. The anti-solvent (chlorobenzene) was added dropwise to the film about 10 s prior to the end of spinning. The films were immediately annealed at 100 °C for 10 min. For the doctor blade coating process, the precursor solution was added dropwise to the substrate and swiped linearly by a metal blade as depicted in Fig. 1. The optimized 2D films were blade coated on glass substrates held at 80 °C by swiping the precursor solution with the blade at a speed of 10 mm s^{-1}. The gap between the glass substrate and the blade was fixed at 400 μm. The films were immediately annealed at 100 °C for 10 min. The optimized reference 3D FAPbI$_3$ perovskite film

Fig. 1 Schematic illustration of the doctor-blade setup used for the deposition of the 2D PEA$_2$PbI$_4$ and reference 3D FAPbI$_3$ perovskite films.

was also blade coated at a temperature of 90 °C at a blade speed of 40 mm s^{-1} and a fixed gap of 400 μm. The film was annealed at 160 °C for at least 30 min. To convert the 2D perovskite to 3D, the 2D film was dipped in 20 mg mL^{-1} FAI in an IPA solution for ~3 min and then rinsed in IPA for ~30 s in order to wash away the dangling PEA$^+$ ions on the surface of the film and subsequently dried by spinning. No further annealing was needed to drive the 3D conversion to full completion.

Morphological characterization

The scanning electron microscopy (SEM) images were obtained using a FEI Nova Nano SEM 650 instrument with an accelerating voltage of 2–10 kV for the secondary electron images and ~10 kV for the backscattered electron images. The atomic force microscopy (AFM) images were taken using a Bruker NanoScope V instrument in the ScanAsyst mode.

Reflected light micrographs were recorded using an Olympus BX51 M microscope equipped with a ColorView CCD camera and Plan Fluor objectives at 5×, 10× and 50× magnifications.

Structural characterization

The X-ray diffraction experiment was performed under ambient conditions using a Bruker D8 Advance diffractometer operated in the Bragg–Brentano geometry and equipped with a Cu Kα radiation source (λ = 1.54 Å) and a LynxEye detector.

Optical characterization

Absorption measurements were taken using a UV-vis-NIR spectrophotometer (Shimadzu UV-3600). The photoluminescence measurements were performed using the second harmonic (400 nm) of a Ti:sapphire laser (repetition rate, 76 MHz; Mira 900, Coherent) to excite the samples. The illumination power could be adjusted using a variable neutral density filter. The excitation beam was spatially limited using an iris and focused with a 150 mm focal length lens. Emitted photons were collected with a lens and directed to a spectrograph. Steady-state spectra were collected using a Hamamatsu EM-CCD camera.

Confocal laser scanning microscopy (CLSM) measurements were performed using a Nikon Eclipse Ti microscope. Samples were excited using Ar$^+$ ions with an excitation wavelength of 488 nm. The excitation beam was focused on the sample using a 100× (oil immersion Plan Apo) objective. Spatial mapping of the photoluminescence was obtained by raster scanning the sample and recording the PL signal using a 650 nm long pass detection channel.

Results and discussion

2D PEA$_2$PbI$_4$ perovskite thin films are fabricated from a solution containing 2-phenylethylammonium iodide (PEAI) and PbI$_2$ in a solvent mixture of N,N'-dimethylformamide (DMF) and dimethyl sulfoxide (DMSO) using both the spin coating

and doctor-blade coating techniques. Unlike the 3D perovskites, this 2D material exhibited good film formability even when deposited using the one-step solution deposition technique. Fig. 1 shows a schematic diagram of the deposition procedure for the doctor-blade coating technique. The detailed fabrication procedure of the 2D films using both the spin-coating and doctor-blade coating methods is described in the Experimental section.

The structure, morphology and band gap of the prepared thin films are examined using X-ray diffraction (XRD), atomic force microscopy (AFM) and UV-Vis spectroscopy, respectively. The two deposition techniques result in thin films with similar XRD patterns and absorption profiles but very different morphologies. As is shown in Fig. S1a,† the XRD patterns of the two samples exhibit similar diffraction peaks with preferential orientation at 2θ values of 5.45°, 10.88°, 16.30°, 21.79°, 27.29°, 32.92° and 38.56°. However, the doctor-blade coated film exhibits more than three orders of magnitude stronger peak intensity compared to the spin coated film. This proves the higher crystallinity of the doctor-blade coated film.

The absorption spectra of these thin films closely resemble those previously reported with an excitonic peak at 515 nm.[59] The doctor-blade coated film, however, has a higher absorbance than the spin-coated film, implying that the film is thicker and/or has better surface coverage (Fig. S1b†).

The morphological properties of the films are characterized using atomic force microscopy (AFM). While the spin coated film shows high inhomogeneity and roughness with surface grains of nanometer size, the doctor-blade coated film is flatter and smoother and has crystalline domains that are as large as 15 μm as is evident from Fig. S1c and S1d,† respectively. The surface roughness of these films extracted from the AFM images are 22 and 50 nm in favor of the doctor-blade coated film.

The 2D perovskite films are dipped in a solution containing FAI dissolved in isopropyl alcohol (IPA) to convert them into 3D FAPbI$_3$ perovskite by the ion (organic-cation) exchange reaction. The approach follows previous studies, where various 2D perovskites were used as the starting materials to grow multidimensional (2D/3D)[60] or 3D[53,54,58] hybrid perovskites. A schematic diagram of the ion exchange reaction process is depicted in Fig. 2a. Photographs of the 2D perovskite films before and after conversion to 3D films without and with rinsing in IPA are shown in Fig. 2b–d. We observed that without the washing steps in IPA, the 3D perovskite film degrades immediately after drying (Fig. 2c), while the washed samples remain stable for many days. This observation shows that the exchange reaction is kinetically driven, and in the absence of the washing step, it will be thermodynamically driven backwards to the starting material. We therefore attribute this unstable behaviour of the unwashed samples to the presence of long organic ligands on the surface of the film, which readily promotes further reactions that are detrimental to the stability of the converted 3D perovskite film.

To study the kinetics of the cation exchange in more detail, we performed an *in situ* conversion experiment. At time t = 0, a

Fig. 2 (a) Schematic illustration of 2D-to-3D conversion by the cation exchange reaction. (b) Photographs of the spin-dried 2D perovskite film, (c) the converted 3D perovskite film without the washing step in isopropyl alcohol (IPA) and (d) the converted 3D perovskite film with the washing step in IPA.

FAI/IPA ligand solution is injected into a cuvette containing the 2D perovskite film to initiate the 2D-to-3D conversion while simultaneously monitoring the photoluminescence (PL) of the sample. Fig. 3a shows the PL emission evolution of the conversion taken at 1 second time interval. Initially, only a narrow peak of the 2D perovskite at 530 nm is observed. The PL intensity of this 2D peak increases in the first second after adding the ligand solution but then vanishes almost completely within another 10 seconds. At the same time, a much broader PL peak originating from the 3D FAPbI$_3$ emerges around 800 nm. The emission from the 3D perovskite shows a rapid decrease in PL intensity and a considerable red-shift in the first seconds after its appearance. A detailed analysis of the dynamics of the 3D peak can be found in the ESI (Fig. S2a and S2b†). After the appearance of the feature at around 800 nm, a minimum PL intensity is reached after 40 seconds as shown in Fig. S2a.† After this local minimum, the intensity steadily increases again while the peak continues to exhibit a small monotonic red-shift (Fig. S2b†). This red-shift is most likely caused by the conversion of low-dimensional perovskite intermediates to the 3D perovskite phase. It is important to underline that an eventual PL signal from the 2D and other low-dimensional perovskite phases, after the start of the conversion towards the 3D perovskite phase, will not be directly detectable because of reabsorption and energy transfer. The slow recovery of PL in the final stage of the conversion process is considered to be the result of further growth of the 3D domains and minimization of defects through laser-induced healing.

After the full conversion from 2D to 3D, the films are characterized to investigate the quality of the films. The comparison of the converted 3D films based on the spin coated and doctor-blade coated 2D films shows that the latter exhibit

better film properties, mimicking the quality of the 2D films. The structural and morphological characteristics of the converted film based on the spin coated 2D film are shown in Fig. S3 of the ESI.† As a reference for the converted films based on the doctor-blade coated 2D films, 3D FAPbI$_3$ thin films were doctor-blade coated on a glass substrate.

The XRD patterns illustrating the structural properties of the converted and reference 3D perovskite films fabricated by doctor-blade coating are displayed in Fig. 3b. Compared to the reference film, the converted films exhibit highly oriented crystal domains with characteristic peaks at 2θ values of 13.97°, 28.13° and 42.71°, corresponding to scattering from (111), (222) and (333) crystal planes. The reference film, on the other hand, exhibits additional diffraction peaks at 12.74°, 19.79°, 24.30°, 31.56°, 34.65°, 38.81° and 40.22°, which correspond to randomly arranged crystal planes. Although no signature peak of the photoinactive (δ-phase) perovskite is observed in both films, the characteristic peak from PbI$_2$ (12.74°), which is a result of the rapid degradation of the sample in air, is observed in the reference film. The diffraction peaks from the converted films are about two orders of magnitude stronger in intensity than that of the reference film. In Fig. 3b, the peak intensity of the reference film is magnified by a factor of 100 for the purpose of illustration. The FWHM of the characteristic peak at 13.97° is 0.14° and 0.21° for the converted and the reference sample, respectively. This shows that the converted perovskite film has better crystallinity and a lower level of disorder with respect to the reference sample. It's worth mentioning, at this point, that no diffraction peaks from the 2D perovskite are observed in the diffraction pattern of the converted film.

As explained above, the morphological quality of thin films defines the success of a deposition technique. SEM images portraying the film topography (secondary electrons) and the composition (backscattered electrons) of the 2D, converted 3D and the reference 3D perovskite films are shown in Fig. 3. In Fig. 3c, the secondary electron image of the 2D perovskite depicts a continuously smooth and homogeneous film with excellent surface coverage and very large crystalline domains (>10 μm), consistent with that seen in the AFM images. The uniform brightness of the backscattered electron images also reflects the highly uniform compositional distribution of the 2D film (Fig. 3d). These morphological features are directly translated into the converted 3D films except for the domain sizes, which appear smaller (>3 μm), and the presence of pinhole-like features at the domain boundaries as shown in Fig. 3e and f for the secondary electron and backscattered electron images, respectively. SEM images showing a wider view of the converted film are shown in Fig. S4.† The roughness of the converted 3D film as extracted from the AFM topographical image (Fig. S5†) is approximately 40 nm. Interestingly, laser scanning confocal microscopy measurements performed on the converted film show that the pitted domain boundaries have brighter photoluminescence (see Fig. S6†). In stark contrast, the topographical image of the 3D reference film in Fig. 3g shows the formation of hexagonal-like crystalline domains, resulting in a non-uniform film. As revealed in the
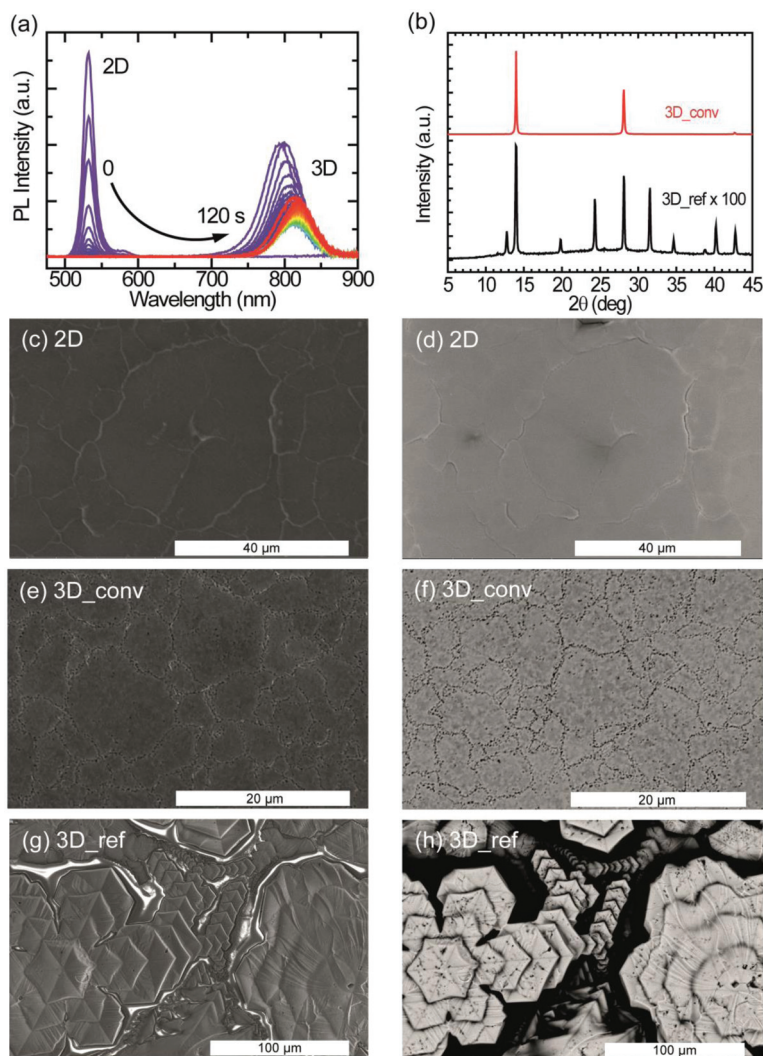
Fig. 3 2D–3D conversion kinetics and structural and morphological characterization of the converted and reference 3D perovskite films, all fabricated by the doctor-blade coating technique. (a) *In situ* photoluminescence (PL) emission spectra showing the conversion kinetics of the evolution from 2D to 3D perovskites, (b) X-ray diffraction patterns of the converted and the reference film fabricated by doctor-blade coating. (c–h) Four SEM images showing the surface topography and compositional properties of the 2D PEA_2PbI_4, the converted and the reference 3D $FAPbI_3$ perovskite films. (c, e and g) Secondary electron and (d, f and h) backscattered electron images of the 2D, converted and reference 3D perovskite films, respectively.

backscattered electron image of Fig. 3h, the surface coverage of the film is very poor.

The absorbance spectra of the converted and reference 3D $FAPbI_3$ perovskite films are shown in Fig. 4a. The spectra are normalized at 840 nm to aid in the comparison of the spectral shape and estimation of the band-edge (see Fig. 4b). The films have an absorption band-edge of around 830 nm, confirming the formation of the 3D $FAPbI_3$ perovskite. However, the spectral profiles of the films are very different. The converted film has a characteristic absorption profile that depicts a continuous increase in light absorption from the near-infrared (NIR) to the visible region while the reference film shows almost constant light absorption in the same range. Moreover, as is shown in Fig. 4a, the reference film has a very high background signal in the NIR region compared to the converted

film. These features are directly related to the film quality, specifically, the degree of surface coverage and homogeneity. While the observed high background absorption from the reference film is attributed to the high inhomogeneity of the film, which gives rise to a large scattering of the incident light, the flattening of the spectrum is attributed to poor surface coverage. These observations are in agreement with previous studies by Tian *et al.*, where the correlations between the absorption spectral shapes and surface coverage and inhomogeneity of $MAPbI_3$ perovskite thin films are examined.[61]

Fig. 4c shows the photoluminescence spectra of both the reference and the converted film upon excitation with a 400 nm laser. The converted film shows a PL intensity that is over 20 times higher than that of the reference film. This large difference in PL intensity has two main causes; firstly, as men-
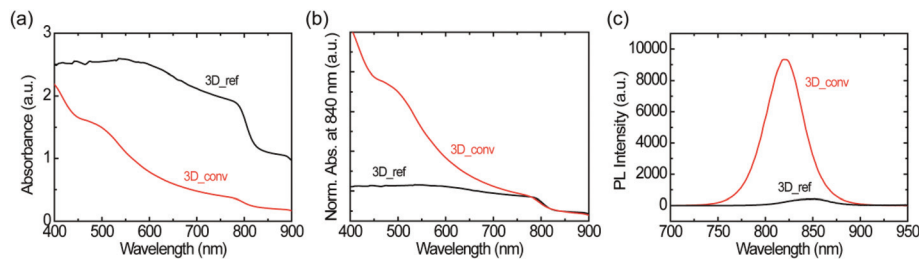
Fig. 4 Optical characterization of converted and reference 3D perovskite films on glass substrates. (a–b) UV-vis absorbance spectra without normalization (a) and with normalization at 840 nm (b), (c) steady-state PL spectra. Note that 3D_ref and 3D_conv as indicated in the figures denote the reference one-step coated and converted FAPbI$_3$ perovskites, respectively.

tioned before, the converted film shows much higher surface coverage than the reference film. Therefore, more photons are absorbed in the converted film and the PL intensity scales accordingly. Secondly, as the quality of the converted film is better than that of the reference film, it is to be expected that the excited charge carriers suffer less from non-radiative recombination in this film. This notion is further confirmed by the large red-shift of the PL spectrum of the reference film (845 nm) with respect to that of the converted film (823 nm); such a red-shift is typically associated with a high density of trap states.[58]

At this point, it is interesting to determine whether the stability of the material is also affected by the preparation method. The stability under ambient conditions is evaluated

by probing the changes in the absorbance of the films under a relative humidity (RH) of 40–50% and a temperature of ~23 °C. It is worth noting that the stability test under ambient conditions is performed on several films and a clear influence of the film degradation over time on the quality of the film is found. Photographs of the most stable converted and reference films stored in air over a period of 21 days are presented in Fig. 5a. Whereas the best reference film degraded rapidly within a day with consequent severe color bleaching, the best converted sample showed minimal degradation with negligible change in color even after 15 days. We attribute the degradation to the penetration of moisture at the grain or domain boundaries. The corresponding absorbance spectra of the films are shown in Fig. 5b and c for the reference and con-
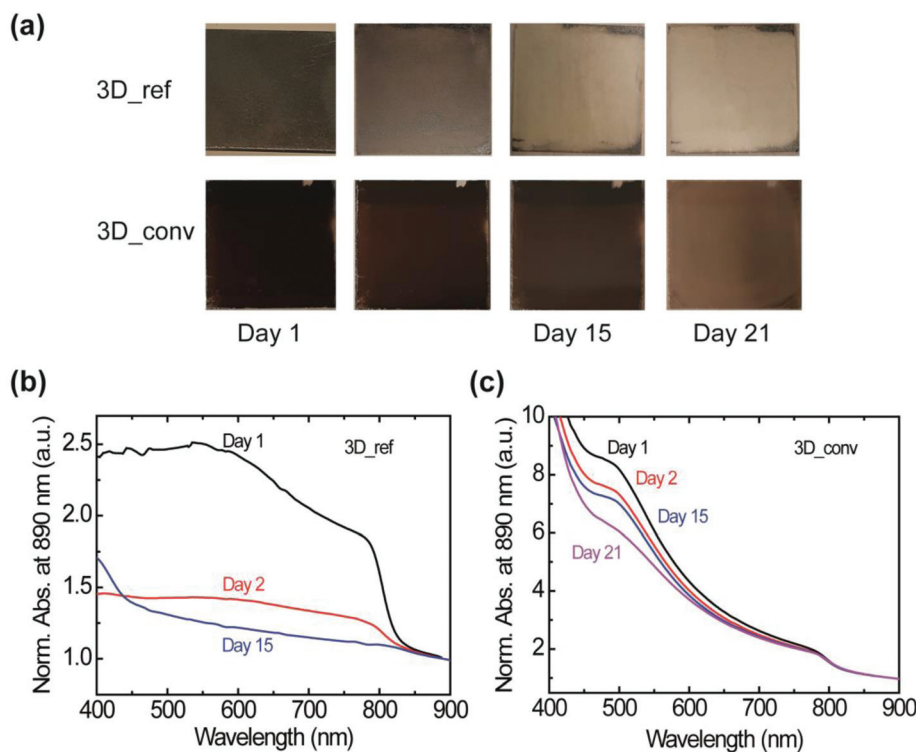

Fig. 5 Characterization of the moisture stability of the reference and converted 3D FAPbI$_3$ perovskite films under ambient conditions. (a) Photographs showing the evolution of the color of the reference (top) and converted (bottom) perovskite films over a 21 day period. (b and c) UV-vis absorbance spectra of the reference (b) and the converted (c) films normalized at 890 nm.
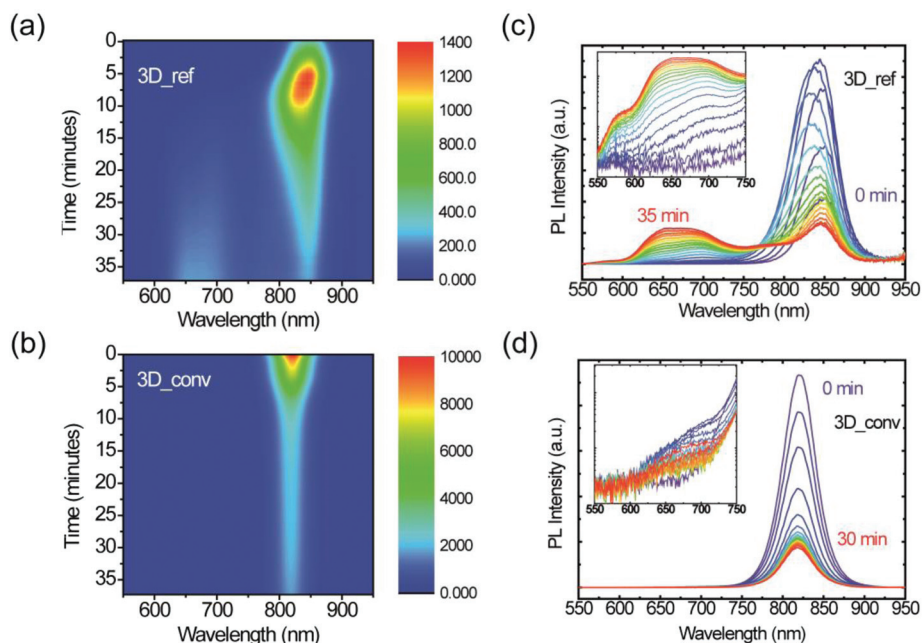
Fig. 6 Photostability of the reference and converted 3D FAPbI₃ perovskite films. (a) 2D pseudo-color plot of the PL spectra of the reference film as a function of continuous laser excitation time. (b) 2D pseudo-color plot of the PL spectra of the converted film as a function of continuous laser excitation time. (c) Evolution of the PL spectra of the reference film. (d) Evolution of the PL spectra of the converted film.

verted films, respectively. The absorbance of the reference film dropped drastically on the second day and as shown, no absorption peak was observed after 15 days. In contrast, the converted film, as already indicated by the photographs, maintained a high absorbance value without spectral modification for 21 days as shown in Fig. 5c.

Furthermore, the stability under illumination of both the converted 3D and reference films was assessed by exposing them to a focused laser beam of 400 nm (2.5 μJ cm⁻²) wavelength under ambient conditions. Fig. 6 displays color maps of the PL spectra as a function of exposure time for (a) the 3D reference sample and (b) the converted film. PL spectra at selected time intervals are plotted alongside (c) and (d). It is evident from these plots that the films behave distinctly differently under illumination. In the case of the reference 3D film, the low PL initially increases due to the laser-induced healing of trap states, which is accompanied by a slight blue-shift of the emission. After this initial healing stage, however, degradation begins and the intensity steadily drops until the signal reaches about 20% of its maximum intensity. During this degradation phase, a broad emission feature gradually arises at high energy, as is highlighted in the inset of Fig. 6c. We assign this feature to degradation products of FAPbI₃, the most likely being PbI₂, resulting from evaporation of the volatile organic cation as observed in the case of MAPbI₃.[62,63] At the laser excitation point, the decomposition of the perovskite is visible to the naked eye as a yellow spot. A cross-polarized light micrograph showing the strong change in birefringence of this degraded spot is shown in the ESI (Fig. S7†). In stark contrast to this, the converted film only shows a steady decrease in PL

intensity and no degradation byproduct can be observed under the same excitation conditions. Moreover, it should be noted that even after prolonged laser illumination, the final PL intensity of the converted film is still considerably higher than the maximal value that the reference film ever reaches, which again highlights the superior quality of the converted films. Furthermore, the substantially higher PL intensity, narrower FWHM and the blue-shifted emission wavelength as shown in Fig. S8† all indicate the superior quality of the converted film with respect to the reference film.

We can therefore conclude that the herein reported conversion mechanism from a highly crystalline 2D film gives rise to highly oriented 3D films with superior ambient and photostability.

Conclusions

In summary, doctor-blade coated 2D 2-phenylethylammonium lead iodide (PEA₂PbI₄) films were employed as a growth template to fabricate high-quality photoactive 3D FAPbI₃ thin films using a cation exchange reaction. The resultant perovskite film exhibits better film formability, excellent surface coverage and improved morphology with crystalline domain sizes as large as ~10 μm. XRD patterns of the converted 3D perovskite film reveal very high crystallinity and a highly preferential orientation that mimics the orientation of the 2D perovskite template. The improved perovskite film leads to enhanced photoluminescence intensity, about 20 times higher than that of the reference one-step blade-coated FAPbI₃ perovskite film.

Furthermore, stability studies under continuous laser illumination and under ambient conditions show that the converted film exhibits significantly enhanced photo- and moisture stability compared to the reference film. The enhanced optoelectronic quality and high stability of the phase-pure $FAPbI_3$ perovskite thin films obtained by the cation exchange reaction of a doctor-blade coated thin film are of extreme importance for the engineering and stabilization of perovskite thin films for optoelectronic applications.

Conflicts of interest

There are no conflicts to declare.

Acknowledgements

Notes and references

1 M. M. Lee, J. Teuscher, T. Miyasaka, T. N. Murakami and H. J. Snaith, *Science*, 2012, **338**, 643–647.
2 J. H. Noh, S. H. Im, J. H. Heo, T. N. Mandal and S. Il Seok, *Nano Lett.*, 2013, **13**, 1764–1769.
3 G. E. Eperon, S. D. Stranks, C. Menelaou, M. B. Johnston, L. M. Herz and H. J. Snaith, *Energy Environ. Sci.*, 2014, **7**, 982–988.
4 G. Xing, N. Mathews, S. Sun, S. S. Lim, Y. M. Lam, M. Gratzel, S. Mhaisalkar and T. C. Sum, *Science*, 2013, **342**, 344–347.
5 A. Kojima, K. Teshima, Y. Shirai and T. Miyasaka, *J. Am. Chem. Soc.*, 2009, **131**, 6050–6051.
6 B. G. H. M. Groeneveld, M. Najafi, B. Steensma, S. Adjokatse, H.-H. Fang, F. Jahani, L. Qiu, G. H. ten Brink, J. C. Hummelen and M. A. Loi, *APL Mater.*, 2017, **5**, 076103.
7 S. Shao, M. Abdu-Aguye, T. S. Sherkar, H.-H. Fang, S. Adjokatse, G. ten Brink, B. J. Kooi, L. J. A. Koster and M. A. Loi, *Adv. Funct. Mater.*, 2016, **26**, 8094–8102.
8 S. Shao, Z. Chen, H.-H. Fang, G. H. Ten Brink, D. Bartesaghi, S. Adjokatse, L. J. A. Koster, B. J. Kooi, A. Facchetti and M. A. Loi, *J. Mater. Chem. A*, 2015, **4**, 2419–2426.
9 Research Cell Efficiency Records. National Renewable Energy Laboratory. https://www.nrel.gov/pv/assets/pdfs/pv-

efficiency-chart.20181214.pdf, 2018, (accessed on 16 Dec 2018).
10 G. Li, Z.-K. Tan, D. Di, M. L. Lai, L. Jiang, J. H.-W. Lim, R. H. Friend and N. C. Greenham, *Nano Lett.*, 2015, **15**, 2640–2644.
11 O. A. Jaramillo-Quintero, R. S. Sánchez, M. Rincón and I. Mora-Sero, *J. Phys. Chem. Lett.*, 2015, **6**, 1883–1890.
12 Z.-K. Tan, R. S. Moghaddam, M. L. Lai, P. Docampo, R. Higler, F. Deschler, M. Price, A. Sadhanala, L. M. Pazos, D. Credgington, F. Hanusch, T. Bein, H. J. Snaith and R. H. Friend, *Nat. Nanotechnol.*, 2014, **9**, 1–6.
13 X. Y. Chin, D. Cortecchia, J. Yin, A. Bruno and C. Soci, *Nat. Commun.*, 2015, **6**, 1–9.
14 F. Li, C. Ma, H. Wang, W. Hu, W. Yu, A. D. Sheikh and T. Wu, *Nat. Commun.*, 2015, **6**, 8238.
15 F. Maddalena, X. Y. Chin, D. Cortecchia, A. Bruno and C. Soci, *ACS Appl. Mater. Interfaces*, 2018, **10**, 37316–37325.
16 M. U. Chaudhry, K. Tetzner, Y.-H. Lin, S. Nam, C. Pearson, C. Groves, M. C. Petty, T. D. Anthopoulos and D. D. C. Bradley, *ACS Appl. Mater. Interfaces*, 2018, **10**, 18445–18449.
17 S. Chen, K. Roh, J. Lee, W. K. Chong, Y. Lu, N. Mathews, T. C. Sum and A. Nurmikko, *ACS Nano*, 2016, **10**, 3959–3967.
18 Y. J. Li, Y. Lv, C.-L. Zou, W. Zhang, J. Yao and Y. S. Zhao, *J. Am. Chem. Soc.*, 2016, **138**, 2122–2125.
19 H. Zhu, Y. Fu, F. Meng, X. Wu, Z. Gong, Q. Ding, M. V. Gustafsson, M. T. Trinh, S. Jin and X.-Y. Zhu, *Nat. Mater.*, 2015, **14**, 636–642.
20 P. Brenner, M. Stulz, D. Kapp, T. Abzieher, U. W. Paetzold, A. Quintilla, I. A. Howard, H. Kalt and U. Lemmer, *Appl. Phys. Lett.*, 2016, **109**, 141106.
21 S. Yakunin, L. Protesescu, F. Krieg, M. I. Bodnarchuk, G. Nedelcu, M. Humer, G. De Luca, M. Fiebig, W. Heiss and M. V. Kovalenko, *Nat. Commun.*, 2015, **6**, 8056.
22 C. Li, C. Han, Y. Zhang, Z. Zang, M. Wang, X. Tang and J. Du, *Sol. Energy Mater. Sol. Cells*, 2017, **172**, 341–346.
23 H. Lu, W. Tian, F. Cao, Y. Ma, B. Gu and L. Li, *Adv. Funct. Mater.*, 2016, **26**, 1296–1302.
24 H. Sun, T. Lei, W. Tian, F. Cao, J. Xiong and L. Li, *Small*, 2017, **13**, 1701042.
25 Y. Fang and J. Huang, *Adv. Mater.*, 2015, **27**, 2804–2810.
26 S. Yakunin, M. Sytnyk, D. Kriegner, S. Shrestha, M. Richter, G. J. Matt, H. Azimi, C. J. Brabec, J. Stangl, M. V. Kovalenko and W. Heiss, *Nat. Photonics*, 2015, **9**, 444–U44.
27 H. Wei, Y. Fang, P. Mulligan, W. Chuirazzi, H.-H. Fang, C. Wang, B. R. Ecker, Y. Gao, M. A. Loi, L. Cao and J. Huang, *Nat. Photonics*, 2016, **10**, 333–339.
28 A. Kojima, K. Teshima, Y. Shirai and T. Miyasaka, *J. Am. Chem. Soc.*, 2009, **131**, 6050–6051.
29 F. Liu, Q. Dong, M. K. Wong, A. B. Djurišić, A. Ng, Z. Ren, Q. Shen, C. Surya, W. K. Chan, J. Wang, A. M. C. Ng, C. Liao, H. Li, K. Shih, C. Wei, H. Su and J. Dai, *Adv. Energy Mater.*, 2016, **6**, 1502206.
30 J. Burschka, N. Pellet, S.-J. Moon, R. Humphry-Baker, P. Gao, M. K. Nazeeruddin and M. Grätzel, *Nature*, 2013, **499**, 316–319.

31 Z. Xiao, C. Bi, Y. Shao, Q. Dong, Q. Wang, Y. Yuan, C. Wang, Y. Gao and J. Huang, *Energy Environ. Sci.*, 2014, **7**, 2619–2623.

32 Q. Chen, H. Zhou, Z. Hong, S. Luo, H.-S. Duan, H.-H. Wang, Y. Liu, G. Li and Y. Yang, *J. Am. Chem. Soc.*, 2014, **136**, 622–625.

33 M. Liu, M. B. Johnston and H. J. Snaith, *Nature*, 2013, **501**, 395–398.

34 C.-W. Chen, H.-W. Kang, S.-Y. Hsiao, P.-F. Yang, K.-M. Chiang and H.-W. Lin, *Adv. Mater.*, 2014, **26**, 6647–6652.

35 N. J. Jeon, J. H. Noh, Y. C. Kim, W. S. Yang, S. Ryu and S. Il Seok, *Nat. Mater.*, 2014, **13**, 1–7.

36 Y. Rong, Z. Tang, Y. Zhao, X. Zhong, S. Venkatesan, H. Graham, M. Patton, Y. Jing, A. M. Guloy and Y. Yao, *Nanoscale*, 2015, **7**, 10595–10599.

37 Y. Ren, B. Duan, Y. Xu, Y. Huang, Z. Li, L. Hu, T. Hayat, H. Wang, J. Zhu and S. Dai, *Sci. China Mater.*, 2017, **60**, 392–398.

38 J. A. Love, S. D. Collins, I. Nagao, S. Mukherjee, H. Ade, G. C. Bazan and T. Q. Nguyen, *Adv. Mater.*, 2014, **26**, 7308–7316.

39 Y.-K. Ren, X.-H. Ding, Y.-H. Wu, J. Zhu, T. Hayat, A. Alsaedi, Y.-F. Xu, Z.-Q. Li, S.-F. Yang and S.-Y. Dai, *J. Mater. Chem. A*, 2017, **5**, 20327–20333.

40 D. Shi, V. Adinolfi, R. Comin, M. Yuan, E. Alarousu, A. Buin, Y. Chen, S. Hoogland, A. Rothenberger, K. Katsiev, Y. Losovyj, X. Zhang, P. A. Dowben, O. F. Mohammed, E. H. Sargent and O. M. Bakr, *Science*, 2015, **347**, 519–522.

41 Z. Xiao, Q. Dong, C. Bi, Y. Shao, Y. Yuan and J. Huang, *Adv. Mater.*, 2014, **26**, 6503–6509.

42 W. Nie, H. Tsai, R. Asadpour, A. J. Neukirch, G. Gupta, J. J. Crochet, M. Chhowalla, S. Tretiak, M. a Alam and H. Wang, *Science*, 2015, **347**, 522–525.

43 G. E. Eperon, C. E. Beck and H. J. Snaith, *Mater. Horiz.*, 2016, **3**, 63–71.

44 Y. Wu, A. Islam, X. Yang, C. Qin, J. Liu, K. Zhang, W. Peng and L. Han, *Energy Environ. Sci.*, 2014, **7**, 2934.

45 M. Hu, L. Liu, A. Mei, Y. Yang, T. Liu and H. Han, *J. Mater. Chem. A*, 2014, **2**, 17115–17121.

46 L. Hu, J. Peng, W. Wang, Z. Xia, J. Yuan, J. Lu, X. Huang, W. Ma, H. Song, W. Chen, Y.-B. Cheng and J. Tang, *ACS Photonics*, 2014, **1**, 547–553.

47 A. Binek, F. C. Hanusch, P. Docampo and T. Bein, *J. Phys. Chem. Lett.*, 2015, **6**, 1249–1253.

48 D. B. Mitzi, *Progress in inorganic chemistry*, John Wiley & Sons, Inc., 1999, vol. 48.

49 Z. Li, M. Yang, J.-S. Park, S.-H. Wei, J. J. Berry and K. Zhu, *Chem. Mater.*, 2016, **28**, 284–292.

50 C. E. Harland, *Ion Exchange: Theory and Practice*, Royal Society of Chemistry, Cambridge, 1994.

51 S. Pang, Y. Zhou, Z. Wang, M. Yang, A. R. Krause, Z. Zhou, K. Zhu, N. P. Padture and G. Cui, *J. Am. Chem. Soc.*, 2016, **138**, 750–753.

52 Y. Zong, Y. Zhou, M. Ju, H. F. Garces, A. R. Krause, F. Ji, G. Cui, X. C. Zeng, N. P. Padture and S. Pang, *Angew. Chem., Int. Ed.*, 2016, **55**, 14723–14727.

53 F. Li, Y. Zhang, K.-J. Jiang, C. Zhang, J.-H. Huang, H. Wang, H. Fan, P. Wang, Y. Chen, W. Zhao, X. Li, L.-M. Yang, Y. Song and Y. Li, *Adv. Mater.*, 2018, **30**, 1804454.

54 Y. Zhang, F. Li, K.-J. Jiang, J.-H. Huang, H. Wang, H. Fan, P. Wang, C.-M. Liu, L.-P. Zhang and Y. Song, *J. Mater. Chem. A*, 2018, **6**, 17867–17873.

55 Z. Zhou, S. Pang, F. Ji, B. Zhang and G. Cui, *Chem. Commun.*, 2016, **52**, 3828–3831.

56 Y. Zhou, M. Yang, S. Pang, K. Zhu and N. P. Padture, *J. Am. Chem. Soc.*, 2016, **138**, 5535–5538.

57 G. E. Eperon and D. S. Ginger, *ACS Energy Lett.*, 2017, **2**, 1190–1196.

58 T. Zhao, H. Liu, M. E. Ziffer, A. Rajagopal, L. Zuo, D. S. Ginger, X. Li and A. K. Y. Jen, *ACS Energy Lett.*, 2018, **3**, 1662–1669.

59 K. T. Cho, G. Grancini, Y. Lee, E. Oveisi, J. Ryu, O. Almora, M. Tschumi, P. A. Schouwink, G. Seo, S. Heo, J. Park, J. Jang, S. Paek, G. Garcia-Belmonte and M. K. Nazeeruddin, *Energy Environ. Sci.*, 2018, **11**, 952–959.

60 T. M. Koh, V. Shanmugam, J. Schlipf, L. Oesinghaus, P. Müller-Buschbaum, N. Ramakrishnan, V. Swamy, N. Mathews, P. P. Boix and S. G. Mhaisalkar, *Adv. Mater.*, 2016, **28**, 3653–3661.

61 Y. Tian and I. G. Scheblykin, *J. Phys. Chem. Lett.*, 2015, **6**, 3466–3470.

62 A. Latini, G. Gigli and A. Ciccioli, *Sustainable Energy Fuels*, 2017, **1**, 1351–1357.

63 E. J. Juarez-Perez, L. K. Ono, M. Maeda, Y. Jiang, Z. Hawash and Y. Qi, *J. Mater. Chem. A*, 2018, **6**, 9604–9612.